Organic photovoltaic cells – promising indoor light harvesters for self-sustainable electronics

*Harrison Ka Hin Lee, Jiaying Wu, Jérémy Barbé, Sagar M. Jain, Sebastian Wood, Emily M. Speller, Zhe Li, Fernando A. Castro, James R. Durrant, and Wing Chung Tsoi**

*Email: w.c.tsoi@swansea.ac.uk

Dr. H. K. H. Lee, Dr. J. Barbé, Dr. S. M. Jain, E. M. Speller, Dr. Z. Li, Prof. J. R. Durrant, Dr. W. C. Tsoi

SPECIFIC, College of Engineering, Bay Campus, Swansea University, Swansea, SA1 8EN, UK

J. Wu, Prof. J. R. Durrant

Department of Chemistry and Centre for Plastic Electronics, Imperial College London, London, SW7 2AZ, UK

Dr. S. Wood, Dr. F. A. Castro

National Physical Laboratory, Hampton Road, Teddington, TW11 0LW, UK

Abstract

Photovoltaic cells are attracting interest for harvesting indoor light for low power consumption wireless electronics such as those required for smart homes and offices, and the Internet of Things. Here, we explore the potential of solution processable, small molecule photovoltaic cells as indoor power sources. By optimizing solvent vapour annealing (SVA) time to the photovoltaic layer, a record power conversion efficiency of over 28 % is achieved under fluorescent lamps of 1000 lux, generating a maximum power density of 78.2 $\mu W/cm^2$ (>10 % efficiency under AM1.5G). This high indoor performance surpasses silicon based photovoltaic cells, and is similar to gallium arsenide photovoltaic cells. Besides, the ratios of the voltage at maximum power point to the open circuit voltage are similar from indoor lighting to one sun condition, which is rare and allows a less power consuming method to track the maximum power point in this broad range of lighting conditions. The effect of SVA time on the device performance can be correlated to a balance between the crystallization and phase separation of the photovoltaic layers. New insight of the effect of SVA time to the device physics under different light levels is also obtained using advanced optoelectronic characterizations.

1. Introduction

Organic photovoltaic (OPV) cells using solution processable small molecule donors have been receiving more attention in recent years due to the following unique features over polymer donors.[1] Unlike polymers which have a batch-to-batch variation in molecular weight distribution during synthesis which can lead to poor device reproducibility,[2] small molecules have a well-defined structure and thus a monodisperse molecular weight which allows easier purification and better reproducibility.[1] Moreover, the power conversion efficiency (PCE) of such cells can now exceed 11 %,[3,4] approaching the highest PCE's (over 13 %) of polymer based OPV cells.[5]

Although the main market of PV is for outdoors, harvesting photons from the sun, the potential of PV, especially low-cost PV, for harvesting energy from indoor light is becoming more attractive because of the rapid growth in potential applications, including in particular providing local power for the Internet of Things (IoT); the industry forecasts 50 billion devices will be connected to the IoT by 2020.[6] IoT allows communication between small electronic devices via networks, in which wireless electronic devices (containing sensors, actuators, etc.) are one of the key components and can lead to next generation smart homes and offices. For these devices, with typically low power consumption (up to milliwatts), harvesting energy from the indoor ambient environment is a key challenge for wireless devices with sustainable operation for months or ideally years.[6] Temperature differences, mechanical motion, radio-frequency irradiation, and visible light are the primary sources of energy available from the ambient environment. It has been suggested that harvesting ambient light using PV is a particularly attractive solution to deal with this challenge.[6,7] PV devices installed indoors (e.g. home, office, supermarket, or manufacturing

line) have the potential to recycle the light from lighting such as fluorescent lamps and light-emitting diodes (LEDs) which mainly emit visible light with relatively low intensities from 200 lux to 1000 lux.[8,9] Due to the much narrower spectrum and lower intensity of indoor light compared with one sun irradiation, the performance of PV devices can be quite different between these two lighting regimes.[10]

Different types of PV devices including silicon, III–V semiconductors, dye-sensitized, organic and perovskite PV cells have been studied under indoor lighting conditions,[10–17] with some of them showing promising indoor performance.[13,15,16] Among them, a wide bandgap III–V semiconductor PV, GaInP, has demonstrated the highest performance to date, with an open-circuit voltage (V_{OC}) approaching 1.2 V, generating 92.7 μW/cm^2 under 1000 lux fluorescent lamps.[13] There have been some studies of OPV devices for indoor applications. Steim et al. showed that the shunt resistance, R_{Sh}, is more critical than series resistance, R_S, to the performance under low light conditions and suggested that a minimum R_{Sh} of 85 kΩcm^2 is required for low light level applications.[18] Later, Lechêne et al. further explored how R_{Sh} and the reverse saturated current, J_0, affect the low light performance and concluded that the absolute value of R_{Sh} required varies for different systems depending on the ratio of J_0 to short-circuit current density (J_{SC}). There are also some demonstrations using OPV for indoor applications including charging a super-capacitor and powering wireless sensor nodes.[19,20] Recently, OPV devices with respectable one sun performance have been shown to yield more than 22% PCE when tested under LEDs illumination.[21] However, despite these advances, the indoor performance of PV devices is still far from the theoretical limit of 50 % PCE for fluorescent lamps and ca. 60 % PCE for LEDs lighting. [22]

Recently, a promising OPV system has emerged using solution processable blends of small molecule donor and fullerene acceptor, namely benzodithiophene terthiophene rhodamine:[6,6]-phenyl-C_{71}-butyric acid methyl ester (BTR:$PC_{71}BM$), showing attractive performance under one sun, with optimum active layer thickness at 250 nm with fill factors (*FF*) up to 77 % and PCE of 9.3 %. The active layer thickness can be further increased to 400 nm without a significant drop in efficiency, attributed to significantly suppressed bimolecular recombination.[23–25] More importantly, it has a high external quantum efficiency (EQE) across the visible spectrum and a high V_{OC}, both essential requirements for efficient indoor PV device performance.[23,26] It is thus apparent that this is a potentially promising material system for indoor PV application, as evaluated in the study reported herein.

The system BTR:$PC_{71}BM$, like other small molecule:fullerene systems, requires additional processing treatment to obtain its best device performance.[1] In this case, solvent vapour annealing (SVA) of the blend films is the additional step used to achieve high efficiency.[23,27] Engmann et al. have demonstrated the importance of choosing the correct solvent for SVA: a solvent in which the active material is moderately soluble, such as tetrahydrofuran (THF), is more suitable for optimizing device performance than a good solubility solvent, such as chloroform.[27] Although several studies have looked at the morphological changes of BTR:$PC_{71}BM$ films with and without SVA, the influence of SVA on the optoelectronic properties of the devices is still unclear.

In this work, we study the effect of the SVA time (using THF) on the BTR:$PC_{71}BM$ layer and the resulting device performance under one sun and indoor lighting conditions. We find that the optimised BTR:$PC_{71}BM$ cell can achieve an outstanding PCE of over 28 % under indoor lighting (together with an attractive PCE under solar illumination).

Additionally, the V_{max} to V_{OC} ratio is stable from low light to high light levels, which is beneficial as it simplifies the tracking of maximum power point. Furthermore, SVA has a significantly weaker effect on the *PCE* of the devices under 1000 lux illumination than that under one sun. The effect of SVA time on the performance of the devices is correlated to the film morphology of the BTR:$PC_{71}BM$ studied by ultraviolet-visible (UV-Vis) absorption, grazing incidence x-ray diffraction (GIXRD), atomic force microscopy (AFM), and photoluminescence (PL). Furthermore, optoelectronic characterization including photocurrent, charge extraction (CE), and transient photovoltage (TPV) measurements over a range of light levels provide significant insight into the effect of SVA time on the device performance, particularly the difference between indoor lighting and one sun conditions.

2. Results and Discussion

2.1 Device performance under a solar simulator and fluorescent lamps

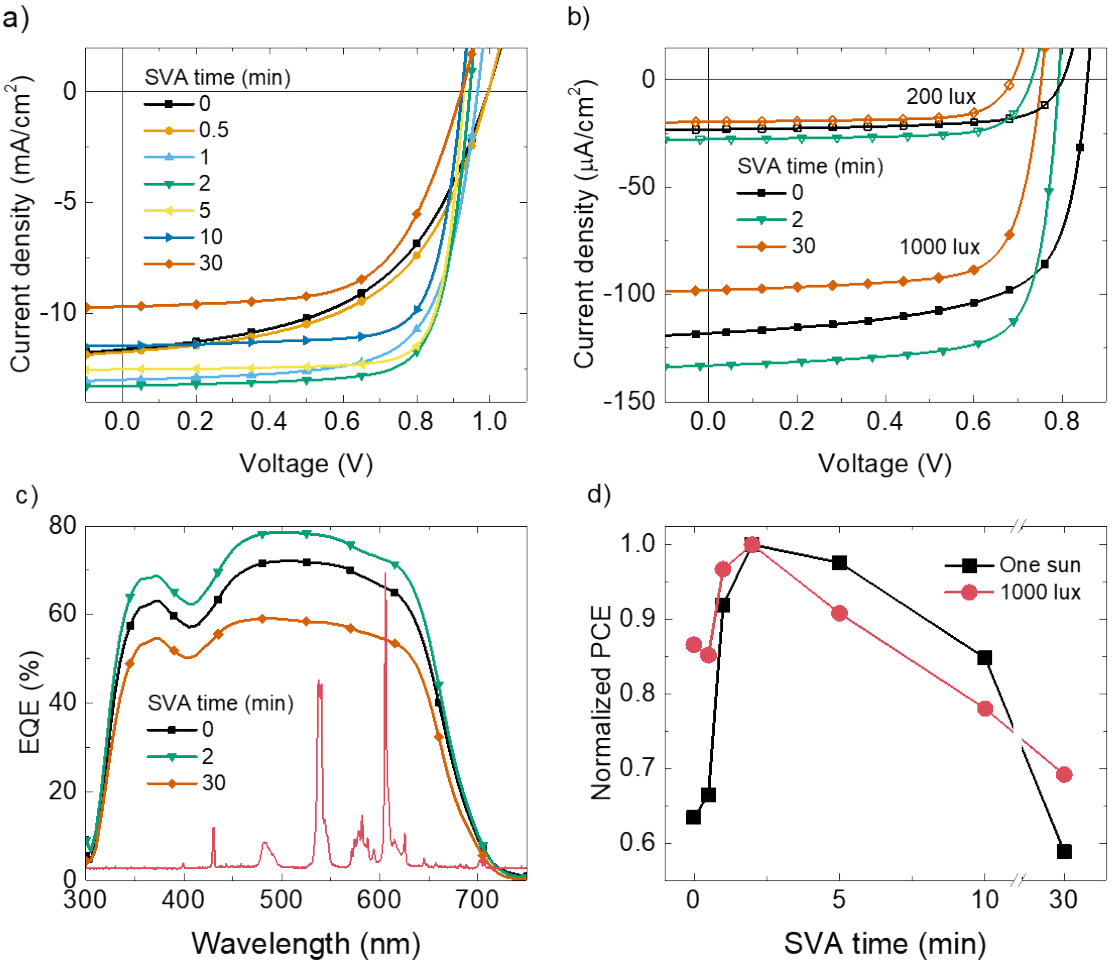

Figure 1 *J-V* characterization for a series of different SVA times, measured under (a) one sun and (b) fluorescent lamps. (c) EQE spectra of the devices with 0 minutes, 2 minutes, and 30 minutes SVA time. Spectrum of the fluorescent lamps is also plotted (arbitrary scale). (d) Normalized PCE measured under one sun and 1000 lux fluorescent lamps for devices with different SVA times.

Table 1 Device parameters for different SVA times, measured under AM1.5G with 90 mW/cm^2 intensity. Values in the brackets are data obtained under 1000 lux fluorescent lamps.

SVA time (min)	J_{SC} (mA/cm^2) [μA/cm^2]	V_{OC} (V)	*FF* (%)	P_{max} (mW/cm^2) [μW/cm^2]	PCE (%)
0	11.6 [118.1]	0.994 [0.856]	51.6 [67.4]	5.97 [6.8]	6.6 [24.2]
0.5	11.8 [117.8]	0.995 [0.859]	53.5 [66.3]	6.26 [66.3]	7.0 [23.8]
1	13.0 [127.0]	0.966 [0.815]	68.9 [73.6]	8.65 [74.8]	9.6 [27.0]
2	**13.3 [133.1]**	**0.945 [0.791]**	**75.1 [75.2]**	**9.42 [78.2]**	**10.5 [28.1]**
5	12.5 [121.8]	0.928 [0.755]	79.1 [77.7]	9.19 [71.0]	10.2 [25.3]
10	11.5 [108.8]	0.923 [0.747]	75.4 [75.6]	7.98 [60.9]	8.9 [21.8]
30	9.7 [98.1]	0.922 [0.754]	61.9 [73.7]	5.54 [53.5]	6.2 [19.3]

The effect of active layer SVA time (from 0 minutes to 30 minutes) on the performance of BTR:$PC_{71}BM$ cells was investigated under both AM1.5G and indoor lighting conditions. **Figure 1a** shows the corresponding current density-voltage (*J*-*V*) characteristics of BTR:$PC_{71}BM$ devices under AM1.5G and the device parameters are listed in **Table 1**. The variation of each device parameter with the SVA time is shown in **Figure S1**. V_{OC} of the devices with no SVA and 0.5 minutes SVA are the highest (approaching 1 V), and it decreases gradually with SVA time, saturating at about 0.92 V from 10 minutes SVA onward. The drop in V_{OC} could be correlated to the improved crystallinity (see section 2.2) of BTR in the blend films upon SVA, as improved crystallization could raise the highest occupied molecular orbital (HOMO) level of the donor,[28] and thus reduce the V_{OC}.[29] The J_{SC} and *FF* increase with SVA time until an optimum time, and then decrease. Moderate SVA times of 2 minutes and 5 minutes result in the highest J_{SC} and *FF* of 13.3 mA/cm^2 and 79.1 %, respectively. Overall, the PCE mainly follows the trend of the J_{SC} and *FF* with SVA time, with the efficiency peaking at 10.5 % (2 minutes SVA) under AM1.5G.

Next, we move to discuss devices tested under an array of fluorescent lamps which mimics a typical indoor environment. **Figure 1b** shows the *J*-*V* curves of 0 minutes,

2 minutes, and 30 minutes SVA obtained under 200 lux and 1000 lux. The device with 2 minutes SVA shows the highest PCE of 26.2 % (200 lux) and 28.1 % (1000 lux), generating a maximum power output density (P_{max}) of 14.6 μW/cm^2 and 78.2 μW/cm^2, respectively. The record high performance can be explained based on our previous work.[26] Firstly, the bandgap of BTR is about 1.8 eV corresponding to the absorption onset of ca. 700 nm (see **Figure 2a** for the absorbance spectra) which is the ideal energy gap to harvest indoor light such as fluorescent lamps and visible light-emitting diodes.[22,30] This is further confirmed by **Figure 1c** which shows that the external quantum efficiency (EQE) spectra of the devices with 0 minutes, 2 minutes and 30 minutes SVA overlap well with that of the fluorescent lamps (also shown in **Figure 1c**) and has a peak EQE of 78.6 % at 515 nm for the device treated with SVA for 2 minutes. Note that the spectrum for the device after 30 minutes SVA shows the lowest EQE and the spectrum for 0 minutes (no SVA) shows an intermediate EQE, consistent with the values of the J_{SC}. Secondly, a high V_{OC} under one sun and high small diode ideality factor η (obtained by measuring the V_{OC} as a function of light intensity), are both beneficial to low light performance.[26] Even if devices behave like an ideal diode (η = 1), there is still an unavoidable voltage drop of 0.15 V to 0.25 V when the light intensity is reduced from one sun to indoor lighting condition, independent of the absolute magnitude of the voltage.[13,14,19,26] The BTR:$PC_{71}BM$ studied herein exhibits a relatively high V_{OC} under one sun (up to 1 V), which minimizes the fraction of the voltage lost at low light intensity. In addition, all the BTR:$PC_{71}BM$ devices measured herein (independent of SVA time) have η values close to the ideal (see **Figure S2**), further enhancing the low light level voltage output.[31]

To compare the effect of SVA time on the device performance under AM1.5G and 1000 lux, PCE under AM1.5G and 1000 lux with different SVA times were normalized to the peak PCE (at 2 minutes SVA), as shown in **Figure 1d**. Interestingly, for short SVA time (0 minutes or 0.5 minutes), the PCE under one sun has only around 65 % of the peak efficiency whereas the PCE under 1000 lux fluorescent lamps maintains 86 % of the peak efficiency. To investigate this difference, device parameters under 1000 lux were compared to those under one sun for different SVA times, as shown in **Figure S1**. From this figure, it is apparent that the *FF* is the main parameter which exhibits the most significant enhancement from AM1.5G to 1000 lux (also less V_{OC} reduction as shown in **Figure S1b**). This enhancement is most pronounced for the 2 minutes SVA device. In order to elucidate the origins of the enhanced performance, and specifically enhanced, obtained under low level irradiation, and why this enhancement is dependent upon SVA time, we further investigated the films and devices in terms of their film morphology and optoelectronic properties in the following sections.

2.2 Effect of SVA on film morphology

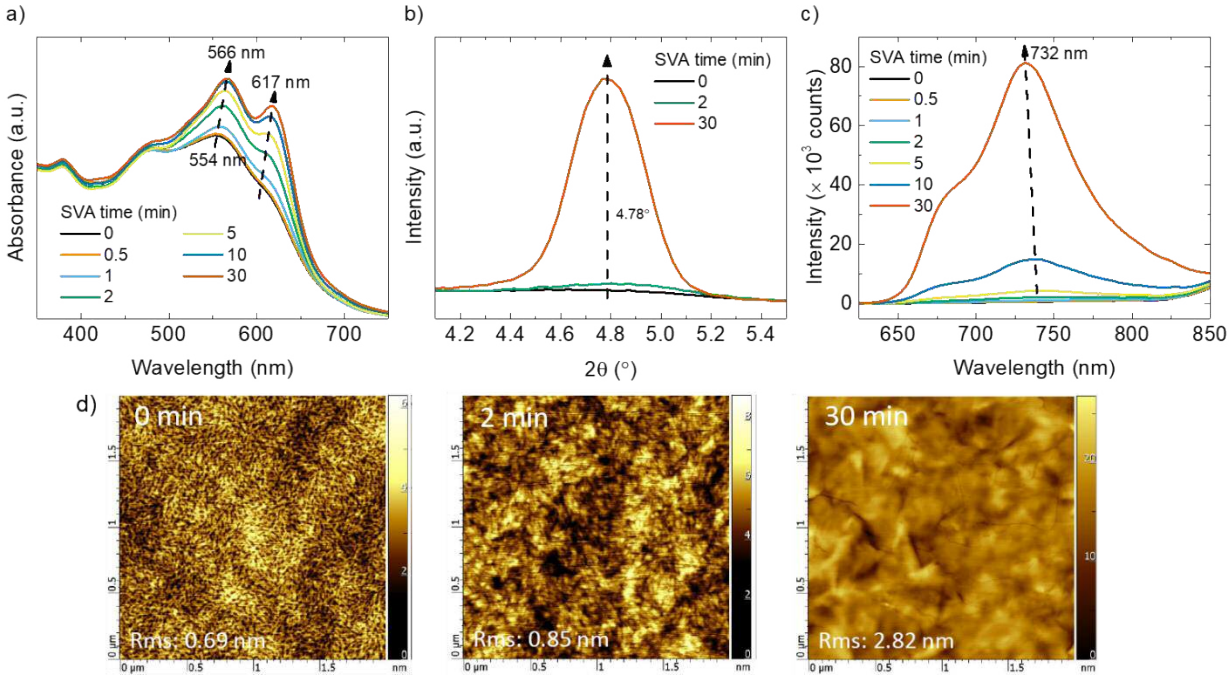

Figure 2 (a) UV-Vis absorption spectra; (b) GIXRD measurement; (c) PL spectra; and (d) AFM topographical images of the BTR:$PC_{71}BM$ blend films with increasing SVA time.

To understand the effect of SVA time on the film morphology and how the morphology correlates to the device performance, UV-Vis absorption, GIXRD, PL and AFM measurements on the BTR:$PC_{71}BM$ blend films were performed. **Figure 2a** shows clearly that the low energy optical absorbance peaks increase in strength with increasing SVA time, along with a red shift observed for both the main peak (from 554 nm to 566 nm, whose strength increased by 31%) and the shoulder (around 617 nm) after 30 minutes SVA. This is consistent with an increase in crystallinity of the BTR phase.[23,27] This assignment is directly supported by the corresponding GIXRD data (**Figure 2b**; see **Figure S3a** for a zoomed-in figure), which has a diffraction peak at $2\theta = 4.78°$ (corresponding to an interlayer spacing of 1.85 nm) whose magnitude increases with increasing SVA time (an approximate 8-fold increase from

0 minutes to 30 minutes. The enhancement in absorbance and greater crystallization can explain the increase in device efficiency for devices with SVA time up to 2 minutes.

To explain the decrease in device efficiency for SVA times longer than 2 minutes, we consider the PL quenching and surface topography of the blend films with different SVA times. The PL intensity (**Figure 2c** and **Figure S3c** for a zoomed-in plot) of the blend film (measuring PL from BTR) increases significantly with longer SVA times: more than 120 times larger when comparing samples with 30 minutes to 0 minutes SVA (for 0 minutes SVA, PL is too weak to be accurately measured). The PL quenching efficiencies are calculated by

for 0 minutes, 2 minutes, and 30 minutes (see **Table S1**), where PL_{blend} is the maximum PL intensity of the BTR:$PC_{71}BM$ blend film and PL_{neat} is the maximum PL intensity of the BTR neat film. The PL quenching is very efficient for short SVA times (> 99% for both 0 and 2 minutes SVA) but decreases to 45% for 30 minutes SVA. This indicates that long SVA times result a substantial loss of exciton separation efficiency, explaining observed the drop in J_{SC} and EQE. Note that the PL peak position is slightly blue shifted (to 732 nm for 30 minutes SVA) with longer SVA times. The much stronger PL quenching with increasing SVA time is further supported by the corresponding AFM images of the blend films, which show an increase in domain size and RMS roughness (0 minutes: 0.69 nm, 2 minutes: 0.85 nm and 30 minutes: 2.82 nm) for longer SVA times. As the domain size increases (indicating more phase separation) due to an increase in crystallization, PL is quenched less efficiently. The PL and AFM results agree well with the decrease in device efficiency when the films are over treated with SVA. Therefore, we propose that the optimum SVA time (2 minutes) represents a balance between the above two opposing effects, i.e. increase in crystallization with SVA and decrease in PL quenching for long SVA.

2.3 Effect of SVA on photoelectrical properties

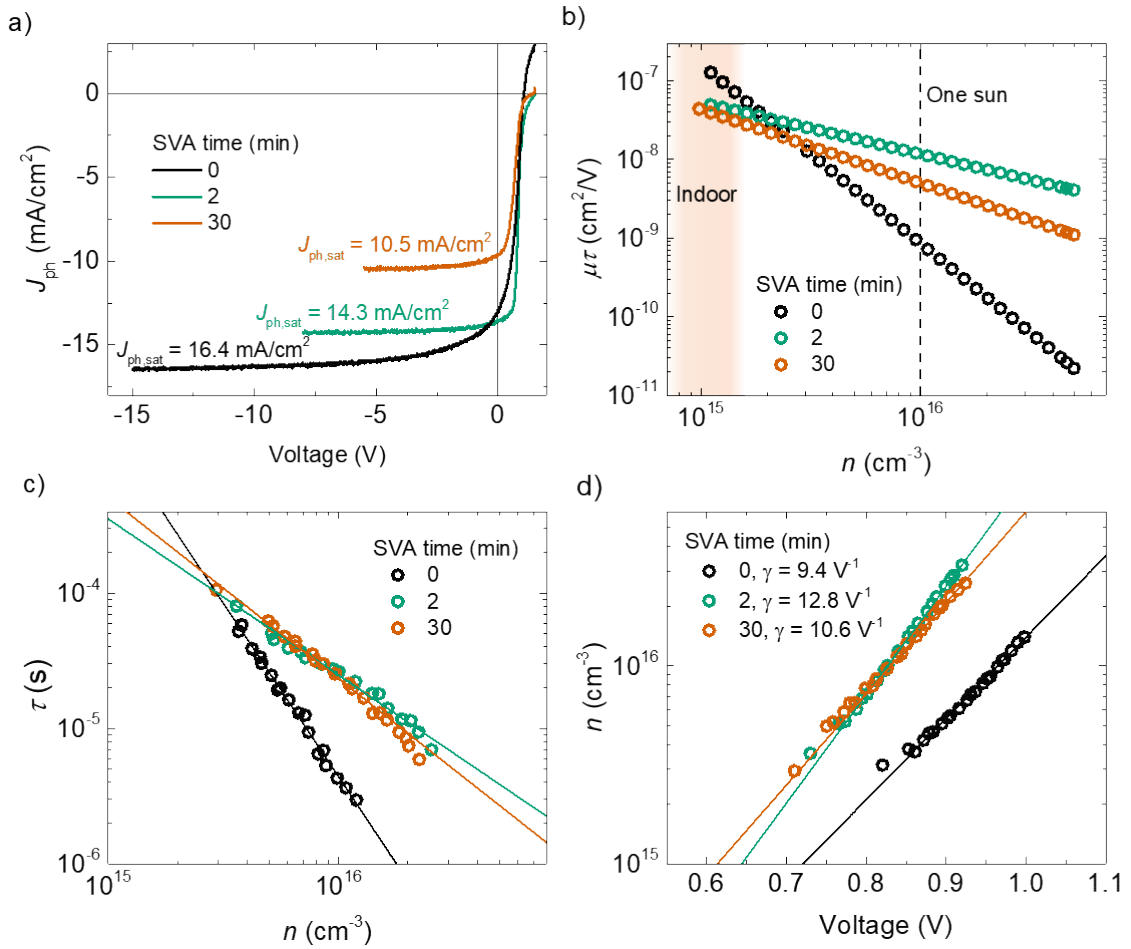

Figure 3 (a) Corrected photocurrent , the saturated J_{ph} at far reverse bias equals the total generation of current without loss. (b) Mobility lifetime product as a function of charge carrier density n, the mobility and lifetime used from the fitted data from short-circuit and open-circuit conditions respectively. (c) Charge carrier lifetime as a function of charge carrier concentration and (d) charge carrier density graph versus voltage.

To understand the effect of SVA time on device performance more quantitatively, further optoelectronic characterization was performed to probe the dynamics of charge generation and collection. To gain insight into the impact of SVA time on photocurrent generation, corrected photocurrent measurements were performed in far reverse bias and shown in **Figure 3a**. By applying a large reverse bias, photo-generated charge carriers are more efficiently extracted by the strong electric field. In principle, if the bias is high enough, all photogenerated charge carriers can overcome recombination resulting in collection without any loss. It can be seen that the device without any SVA process is able to generate

the highest photocurrent: in excess of 16.4 mA/cm^2, compared to 14.3 mA/cm^2 for 2 minutes SVA and 10.5 mA/cm^2 for 30 minutes, the corresponding maximum electron-hole pair generation rates are available in **Table S2**.[32] However, J_{ph} of the 0 minutes SVA device possesses a higher bias dependence, which is distinct from the 2 minutes and 30 minutes cases. The large drop in J_{ph} from 2 minutes to 30 minutes correlates well with the reduced PL quenching efficiency in **Table S1**. However, for the device without SVA, the high J_{ph} at far reverse bias is not maintained at short circuit. For all three devices, under short circuit conditions, current loss due to non-geminate recombination appear negligible, as evidenced by the linear behaviour of short circuit photocurrent with light intensity (see **Table S2** and **Figure S4**) and direct measurements of charge densities and recombination lifetimes as detailed below.[33] As such, the loss of photocurrent for the 0 minutes SVA device, most likely results from field dependent geminate recombination losses; such field dependent recombination losses have been reported previously to be more severe in more amorphous blends.[34]

The improved *FF* under low light implies a more efficient charge carrier collection process. The efficiency of the charge carrier collection process is indicated by the ratio of charge carrier drift length L_{dr} to active layer thickness: —— ——, here μ is the charge carrier mobility, τ is charge carrier lifetime and V_{int} is the internal voltage within the device.[35] The higher this ratio, the better the collection should be for a given device. The collection efficiency of the devices under an electric field can thus be correlated with the $\mu\tau$ product. **Figure 3b** shows the experimental determination of the $\mu\tau$ product over a range of charge carrier concentration (by changing light intensity) from measurements of average drift mobility measured from charge extraction data at short circuit (see **Figure S5**) and

charge carrier lifetime measured from transient photovoltage decays at open circuit (see **Figure 3c**). Note that the 2 minutes SVA device presents the highest mobility among the three devices, ranging from 1×10^{-4} cm^2/Vs to 4×10^{-4} cm^2/Vs. Near the one sun operating condition (the charge carrier concentration at maximum power point (MPP) is around 1×10^{16} cm^{-3} for all three types of device), the $\mu\tau$ products rank 2 minutes > 30 minutes > 0 minutes, which correlates well with the *FF* under AM1.5G.

On the other hand, the charge carrier collection for devices with different SVA times under low light intensity is different from one sun. Due to much stronger negative dependence on the charge carrier density for the device without SVA, the $\mu\tau$ product is superior to that of the SVA treated devices when the charge carrier density is lower than 2×10^{15} cm^{-3} (this is around 1% sun irradiation and equivalent to indoor lighting conditions). The slopes in **Figure 3b** for the three devices could be qualitatively interpreted as the difference in the improvement of the *FF* measured under AM1.5G to indoor light, the steeper the slope the more the improvement observed in *FF* (see **Figure S1**). The difference in the dependence of the $\mu\tau$ product upon light intensity is mainly governed by the increase in charge carrier lifetime with increasing charge carrier density, while the drift mobility is relatively invariant (see **Figure S5**).

Electronic energy level disorder, often observed by the presence of band edge tail (shallow trap) states can lead to differences in the dependence of carrier lifetime upon charge density.[36] The distribution of these tail states can be derived from charge carrier density versus V_{OC} measurements.[36] A typical expression of n as a function of V is

, where the constant quantifies the dependence of charge carrier density upon film quasi-Fermi level splitting. $\gamma \approx 19$ for ideal semiconductors, with smaller values

indicating increasingly broad distributions of tail states. Here we find that in **Figure 3d** the device with 2 minutes treatment shows the largest γ (γ = 12.8 V^{-1}) indicating the least energetic disorder, whilst the device without treatment shows the most disordered (γ = 9.4 V^{-1}) among the three. Also, note that the value obtained for the 2 minutes SVA treated BTR:$PC_{71}BM$ devices is among the highest reported for bulk heterojunction OPV systems.[37–41]

2.4 Comparison with other PV technologies and discussion of potential applications

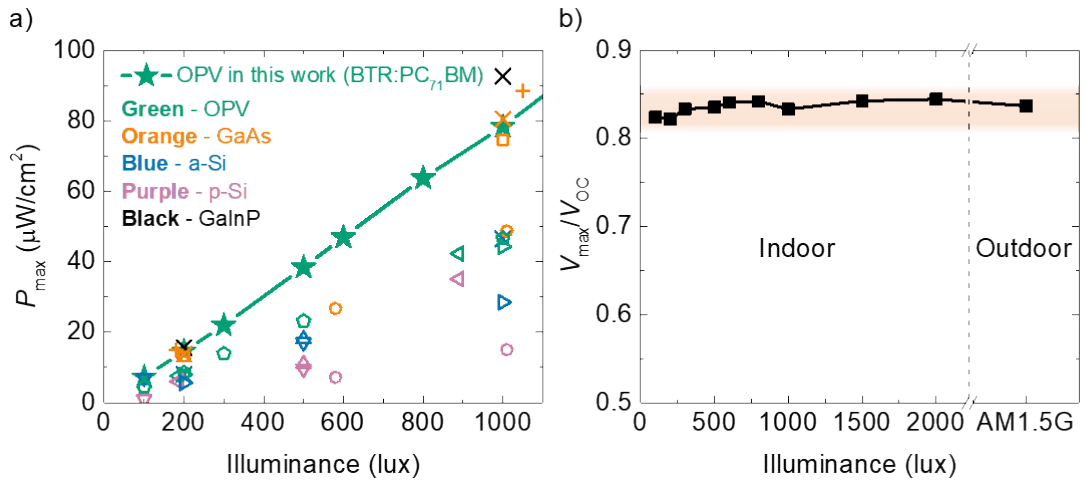

Figure 4 (a) Maximum power density output (P_{max}) of BTR:PC_{71}BM device with 2 minutes SVA at different illuminance and compared to other PV techniques available in the literature. Saltire-cross symbols are from ref.[13] Cross symbols are from ref.[8] Square symbols are from ref.[15] Circle symbols are from ref.[30] Up-triangle symbols are from ref.[11] Down-triangle symbols are from ref.[14] Left-triangle symbols are from ref.[42] Right-triangle symbols are from ref.[20] Pentagon symbols are from ref.[26] (b) Ratio of V_{max} to V_{OC} of the BTR:PC_{71}BM device with 2 minutes SVA from indoor lighting to AM1.5G condition.

A plot of the P_{max} at different illuminance can be useful to determine the cell size needed to obtain a certain power requirement in an indoor environment in which the light level is usually fixed and stable. **Figure 4a** shows the P_{max} obtained by the BTR:PC_{71}BM device with 2 minutes SVA at different illuminance (corresponding *J-V* curves are available in **Figure S6**). The plot of P_{max} against the illuminance shows nearly linear proportionality. We further compare the OPV performance with published values for inorganic PV technologies tested under indoor conditions.[8,11,13–15,20,26,30,42] Obviously, the OPV device reported here not only outperforms polycrystalline-silicon (p-Si) and amorphous-silicon (a-Si) PV cells but also behaves comparably to gallium arsenide (GaAs) PV cells. Moreover, our results also

approach the highest indoor performance reported using gallium indium phosphide (GaInP) as the active material.[13]

Since the absolute power generated under an indoor environment is somewhat lower, a MPP tracking method used for outdoors may not be suitable for indoor applications.[43] The fractional-voltage method is perhaps more appropriate for indoor applications, which employs a pre-set voltage fraction in a circuit to track the MPP and thus consume much less power compared to the MPP tracking method used for outdoors.[44] The voltage fraction is defined by the ratio of the voltage at the MPP (V_{max}) to the V_{OC}, and could vary significantly for different light levels since this ratio is closely related to the *FF*, which changes substantially with the light intensity.[45] We have extracted this ratio for BTR:$PC_{71}BM$ device with 2 minutes SVA as shown in **Figure 4b**. The ratio is surprisingly stable from 100 lux to AM1.5G illumination which can be attributed to the high and stable *FF* throughout this broad range of light levels. Although in most typical cases PV cells may either be used outdoors or indoors, some applications, such as PV cells integrated wearable electronics, may require efficient function under both conditions. This result suggests that circuit design for both indoor and outdoor use can be significantly simplified for the OPV system studied herein.

3. Conclusion

In conclusion, we have studied the performance of BTR:$PC_{71}BM$ devices with SVA times ranging from 0 minutes to 30 minutes under different lighting conditions. With a moderate treatment time of 2 minutes to 5 minutes, we obtain a PCE over 10 % with up to 79 % *FF* under AM1.5G illumination and 78.2 μW/cm^2 power density generated under fluorescent lamps at 1000 lux, translating into a PCE of 28.1 %, the highest OPV performance for indoor applications reported to date. The devices exhibit a stable ratio of V_{max} to V_{OC} from indoor lighting to one sun irradiation, indicating that the fractional-voltage method is ideal for tracking the MPP over a broad range of illumination for these devices. Therefore, the BTR:$PC_{71}BM$ device has promising and unique properties for both indoor and outdoor applications. The effect of SVA treatment on the device performance for both AM1.5G and 1000 lux correlates well with the film morphology (a balance between enhanced crystallization and increased phase separation), and charge generation and collection dynamics, particularly the dependence of mobility-lifetime product on charge carrier density.

4. Experimental Section

Materials: BTR and $PC_{71}BM$ were purchased from 1-Material and Solenne BV, respectively. Chloroform (CF) and anhydrous tetrahydrofuran (THF) are purchased from Sigma-Aldrich. Poly(3,4-ethylenedioxythiophene)-poly(styrenesulfonate) (PEDOT:PSS), Clevios P VP AI 4083, was purchased from Heraeus. All materials were used as received without further purification.

OPV cell fabrication and characterization: Indium tin oxide (ITO) glass substrates (15 Ω/□) were cleaned sequentially with detergent (Hellmanex), deionized water, acetone, and isopropyl alcohol in an ultrasonic bath. BTR and $PC_{71}BM$ (1:1 weight ratio) were dissolved in CF with a total concentration of 40 mg/ml on a 60 °C hotplate stirred overnight in a nitrogen filled glovebox. PEDOT:PSS was first spin-coated (4000 r.p.m. for 60 s) on plasma cleaned ITO glass substrates in air followed by 150 °C annealing on a hotplate for 10 minutes. After transferring the samples to the nitrogen filled glovebox, the blend solution was then spin-coated on the PEDOT:PSS coated substrates at an optimized speed of 1500 r.p.m. for 15 s resulted in ca 220 nm active layer thickness measured by a profilometer. SVA treatment was performed in a sectioned petri dish. THF of 1 ml was put in a section of the petri dish to ensure similar surface area exposed to the solvent vapour environment. The THF filled petri dish was covered with a lid for at least 2 minutes before doing the SVA treatment to the active layer. The samples were placed in the other sections of the petri dish with the active layer facing up for different exposure times as specified in the main text. Finally, 30 nm of calcium and 100 nm of aluminium were thermally evaporated onto the active layer in an evaporator at a based pressure of 2×10^{-5} mbar, forming devices with active area of 0.15 cm^2. All devices were encapsulated with glass slides with the aid of UV-epoxy before

measurements. *J-V* characterizations were performed by a Keithley 2400 sourcemeter under both solar simulator (Newport 92193A-1000) with intensity of ca 90 mW/cm^2 and fluorescent lamps (Osram L18W/827). The lux levels of the fluorescence lamps were measured by a luxmeter, (LX-1330B). The intensity calibration was mentioned in a previous work.[26] EQE spectra were obtained by QEX10 Quantum Efficiency Measurement System.

UV-Vis absorption measurements: The UV-Vis absorbance spectra were measured in the range 200 – 1000 nm using a Perkin Elmer Lambda 750 spectrophotometer. BTR:$PC_{71}BM$ blend films with and without SVA treatment were prepared directly on quartz and a quartz substrate was used as a reference sample for calibration.

GIXRD measurements: GIXRD measurements were carried out using a Bruker D8 Discover instrument with a CuKα beam (wavelength is 0.15418 nm) at 40 kV and 40 mA, scan parameters of 0.1 s/step at 0.01° of 2θ step size.

PL measurements: A FluoroMax-4 spectrofluorometer (Horiba Scientific) was used to measure the photoluminescence spectra of BTR:$PC_{71}BM$ blend films on quartz in the range 560 – 1000 nm using an excitation wavelength of 532 nm. The integration time was 0.2 s. The entrance and exit slits were 5 nm. Diffraction gratings with 1200 gr/mm were used for the excitation and emission monochromators. The spectrum of the lamp was measured by a photodiode located between the sample and the excitation monochromator, and corrected by a calibration file (R1c: corrected lamp spectrum). The emission spectrum S1 were corrected by a calibration file (S1c: corrected emission spectrum) and further divided by the corrected reference signal R1c. The data in the manuscript show the S1c/R1c signal.

AFM measurements: AFM was performed with an AIST-NT CombiScope in non-contact mode using a Budget Sensors Multi75Al-G probe with tip radius < 10 nm. Surface height profiles were levelled by fitting each line with a second order polynomial, before evaluating the root mean square (RMS) roughness values.

Photocurrent/CE/TPV measurements: The corrected photocurrent $J_{ph}(V)$ was measured from the difference in *J-V* response between the dark response $J_{dark}(V)$ and the light response $J_{light}(V)$ by pulsed illumination to avoid overheating the samples. The pulsed illumination was generated by a ring of 12 white LEDs with a fast-switching metal oxide field effect transistor. The one sun equivalent illumination was calibrated by matching the value of J_{SC} obtained under the AM1.5G illumination. The light was switched on for approximately 2 ms to allow the current reaching the steady state and a much longer time was used after switching off the light to avoid the device to cool down. The potential bias was applied by a Keithley 2400 sourcemeter, and the voltage across the device was measured by a Tektronix TDS3032B Oscilloscope with a 1-MΩ input impedance. Charge extraction was used to determine the average charge carrier densities in devices under different illumination levels and under different biases (open circuit and short circuit conditions in this study). The desired light intensity was provided by the ring of 12 white LEDs. The device was held at open circuit under an initial bias with a background light level and then switched to short circuit with the light off simultaneously. The voltage transient was acquired with a DAQ card connected to a Tektronix TDS3032B Oscilloscope. The voltage transients were converted into current transients through Ohms law. The total charges for the calculation of *n* was extracted by integrating the current transients. For the TPV measurements, the device was held at open circuit condition under different background light intensity controlled by the ring of white

LEDs. A small additional optical excitation provided by a pulsed Continuum Minilite Nd:YAG laser at 532nm with a pulse width of < 10 nm was applied to the device under measurement. This small excitation generated a small voltage decay transient which was captured by an oscilloscope. The decay was fitted with a mono-exponential model to obtain the small perturbation carrier lifetime and finally to be used to estimate the total charge carrier lifetime within the device.

Acknowledgements

The authors would like to acknowledge the funding support from the Welsh Assembly Government funded Sêr Cymru Solar Project, EPSRC (grant no. EP/M025020/1), the European Union's Horizon 2020 research and innovation programme under the Marie Skłodowska-Curie grant agreement no. 663830, National Research Network in Advanced Engineering Materials (grant no. NRN093), and the Welsh Assembly Government Sêr Cymru II fellowship scheme.

References

1. Collins, S. D., Ran, N. A., Heiber, M. C. & Nguyen, T. Q. Small is Powerful: Recent Progress in Solution-Processed Small Molecule Solar Cells. *Adv. Energy Mater.* **7,** 1602242 (2017).

2. Lee, H. K. H. *et al.* Batch-to-batch variation of polymeric photovoltaic materials: Its origin and impacts on charge carrier transport and device performances. *Adv. Energy Mater.* **4,** 1400768 (2014).

3. Deng, D. *et al.* Fluorination-enabled optimal morphology leads to over 11% efficiency for inverted small-molecule organic solar cells. *Nat. Commun.* **7,** 13740 (2016).

4. Wan, J. *et al.* Highly efficient halogen-free solvent processed small-molecule organic solar cells enabled by material design and device engineering. *Energy Environ. Sci.* 7992–7995 (2017). doi:10.1039/C7EE00805H

5. Zhao, W. *et al.* Molecular Optimization Enables over 13% Efficiency in Organic Solar Cells. *J. Am. Chem. Soc.* **139,** 7148–7151 (2017).

6. Jayakumar, H. *et al.* Powering the Internet of Things. in *Proceedings of the 2014 International Symposium on Low Power Electronics and Design* 375–380 (2014). doi:10.1145/2491185.2491191

7. Matiko, J. W., Grabham, N. J., Beeby, S. P. & Tudor, M. J. Review of the application of energy harvesting in buildings. *Meas. Sci. Technol.* **25,** 12002 (2014).

8. Mathews, I., Kelly, G., King, P. J. & Frizzell, R. GaAs solar cells for Indoor Light Harvesting. in *2014 IEEE 40th Photovoltaic Specialist Conference* 0510–0513 (2014). doi:10.1109/PVSC.2014.6924971

9. Indoor Dye Sensitized Solar Cells. Available at: http://gcell.com/dye-sensitized-solar-cells/advantages-of-dscc/indoor-dye-sensitize-solar-cells.

10. Reich, N. H., van Sark, W. G. J. H. M. & Turkenburg, W. C. Charge yield potential of indoor-operated solar cells incorporated into Product Integrated Photovoltaic (PIPV). *Renew. Energy* **36,** 642–647 (2011).

11. Li, Y., Grabham, N. J., Beeby, S. P. & Tudor, M. J. The effect of the type of illumination on the energy harvesting performance of solar cells. *Sol. Energy* **111,** 21–29 (2015).

12. Teran, A. S. *et al.* Energy Harvesting for GaAs Photovoltaics Under Low-Flux Indoor Lighting Conditions. *IEEE Trans. Electron Devices* **63,** 2820–2825 (2016).

13. Mathews, I., King, P. J., Stafford, F. & Frizzell, R. Performance of III – V Solar Cells as Indoor Light Energy Harvesters. *IEEE J. Photovoltaics* **6,** 230–235 (2016).

14. De Rossi, F., Pontecorvo, T. & Brown, T. M. Characterization of photovoltaic devices for indoor light harvesting and customization of flexible dye solar cells to deliver superior efficiency under artificial lighting. *Appl. Energy* **156,** 413–422 (2015).

15. Freitag, M. *et al.* Dye-sensitized solar cells for efficient power generation under ambient lighting. *Nat Phot.* **11,** 372–378 (2017).

16. Chen, C. Y. *et al.* Perovskite Photovoltaics for Dim-Light Applications. *Adv. Funct. Mater.* **25,** 7064–7070 (2015).

17. Di Giacomo, F. *et al.* Mesoporous perovskite solar cells and the role of nanoscale compact layers for remarkable all-round high efficiency under both indoor and outdoor illumination. *Nano Energy* **30,** 460–469 (2016).

18. Steim, R. *et al.* Organic photovoltaics for low light applications. *Sol. Energy Mater. Sol. Cells* **95,** 3256–3261 (2011).

19. Lechêne, B. P. *et al.* Organic solar cells and fully printed super-capacitors optimized for indoor light energy harvesting. *Nano Energy* **26,** 631–640 (2016).

20. Aoki, Y. Organic Photovoltaics for energy harvester of wireless sensor network. *Org. Electron.* **48,** 1123–1125 (2017).

21. Cutting, C. L., Bag, M. & Venkataraman, D. Indoor Light Recycling: A New Home for Organic Photovoltaics. *J. Mater. Chem. C* **4,** 10367–10370 (2016).

22. Müller, M. F., Freunek, M. & Reindl, L. M. Maximum efficiencies of indoor photovoltaic devices. *IEEE J. Photovoltaics* **3,** 59–64 (2013).

23. Sun, K. *et al.* A molecular nematic liquid crystalline material for high-performance organic photovoltaics. *Nat. Commun.* **6,** 6013 (2015).

24. Armin, A. *et al.* Reduced Recombination in High Efficiency Molecular Nematic Liquid Crystalline: Fullerene Solar Cells. *Adv. Energy Mater.* **6,** 1–10 (2016).

25. Schwarz, K. N., Geraghty, P. B., Jones, D. J., Smith, T. A. & Ghiggino, K. P. Suppressing Subnanosecond Bimolecular Charge Recombination in a High-Performance Organic Photovoltaic Material. *J. Phys. Chem. C* **120,** 24002–24010 (2016).

26. Lee, H. K. H., Li, Z., Durrant, J. R. & Tsoi, W. C. Is organic photovoltaics promising for indoor applications? *Appl. Phys. Lett.* **108,** 253301 (2016).

27. Engmann, S. *et al.* Film morphology evolution during solvent vapor annealing of highly efficient small molecule donor/acceptor blends. *J. Mater. Chem. A* **4,** 15511–15521 (2016).

28. Tsoi, W. C. *et al.* Effect of Crystallization on the Electronic Energy Levels and Thin Film Morphology of P3HT: PCBM Blends. *Macromolecules* **44,** 2944–2952 (2011).

29. Vandewal, K. *et al.* The relation between open-circuit voltage and the onset of photocurrent generation by charge-transfer absorption in polymer: Fullerene bulk heterojunction solar cells. *Adv. Funct. Mater.* **18,** 2064–2070 (2008).

30. Teran, A. S. *et al.* AlGaAs Photovoltaics for Indoor Energy Harvesting in mm-Scale Wireless Sensor Nodes. *IEEE Trans. Electron Devices* **62,** 2170–2175 (2015).

31. Cowan, S. R., Roy, a & Heeger, a J. Recombination in polymer-fullerene bulk heterojunction solar cells. *Phys. Rev. B* **82,** 245207 (2010).

32. Mihailetchi, V. D., Xie, H., De Boer, B., Koster, L. J. A. & Blom, P. W. M. Charge transport and photocurrent generation in poly(3-hexylthiophene): Methanofullerene bulk-heterojunction solar cells. *Adv. Funct. Mater.* **16,** 699–708 (2006).

33. Stolterfoht, M. *et al.* Photocarrier drift distance in organic solar cells and photodetectors. *Sci. Rep.* **5,** 9949 (2015).

34. Credgington, D., Jamieson, F. C., Walker, B., Nguyen, T. Q. & Durrant, J. R. Quantification of

geminate and non-geminate recombination losses within a solution-processed small-molecule bulk heterojunction solar cell. *Adv. Mater.* **24,** 2135–2141 (2012).

35. Dibb, G. F. A. *et al.* Influence of doping on charge carrier collection in normal and inverted geometry polymer:fullerene solar cells. *Sci. Rep.* **3,** 3335 (2013).

36. Kirchartz, T. & Nelson, J. Meaning of reaction orders in polymer:fullerene solar cells. *Phys. Rev. B - Condens. Matter Mater. Phys.* **86,** 1–12 (2012).

37. Melianas, A. *et al.* Photo-generated carriers lose energy during extraction from polymer-fullerene solar cells. *Nat. Commun.* **6,** 8778 (2015).

38. Deledalle, F. *et al.* Understanding the effect of unintentional doping on transport optimization and analysis in efficient organic bulk-heterojunction solar cells. *Phys. Rev. X* **5,** 1–13 (2015).

39. Wheeler, S. *et al.* Influence of Surface Recombination on Charge-Carrier Kinetics in Organic Bulk Heterojunction Solar Cells with Nickel Oxide Interlayers. *Phys. Rev. Appl.* **4,** 29–31 (2015).

40. Credgington, D. & Durrant, J. R. Insights from transient optoelectronic analyses on the open-circuit voltage of organic solar cells. *J. Phys. Chem. Lett.* **3,** 1465–1478 (2012).

41. Shuttle, C. G. *et al.* Experimental determination of the rate law for charge carrier decay in a polythiophene: Fullerene solar cell. *Appl. Phys. Lett.* **92,** 2006–2009 (2008).

42. Mori, S. *et al.* Investigation of the organic solar cell characteristics for indoor LED light applications. *Jpn. J. Appl. Phys.* **54,** 71602 (2015).

43. Femia, N., Petrone, G., Spagnuolo, G. & Vitelli, M. Optimization of perturb and observe maximum power point tracking method. *IEEE Trans. Power Electron.* **20,** 963–973 (2005).

44. Wang, W. S. *et al.* Design considerations of sub-mW indoor light energy harvesting for wireless sensor systems. *ACM J. Emerg. Technol. Comput. Syst.* **6,** 1–26 (2010).

45. Bartesaghi, D. *et al.* Competition between recombination and extraction of free charges determines the fill factor of organic solar cells. *Nat. Commun.* **6,** 7083 (2015).